A novel Terrain Correction Sinusoidal Model for improving estimation of daily clear-sky downward shortwave radiation

Hui Liang, Bo Jiang, *Member, IEEE*, Shunlin Liang, *Fellow, IEEE*, Jianguang Wen, Tao He, *Senior Member, IEEE*, Xiaotong Zhang, Jianghai Peng, Shaopeng Li, Jiakun Han, Xiuwan Yin

***Abstract*—Downward shortwave radiation (DSR) is greatly affected by rugged terrains, which account for about 24% of the world's surface. Yet, existing DSR products do not take into account topographical effects. Some topographic correction algorithms have been developed for estimating the clear-sky instantaneous DSR over rugged terrains ($DSR_{ins\text{-}rugged}$), but no specific algorithms are available to get the daily average DSR over rugged terrains ($DSR_{daily\text{-}rugged}$). The objective of this study is to develop an efficient and robust model to retrieve the clear-sky $DSR_{daily\text{-}rugged}$ based on DSR satellite products. After examining ground measurements collected from several mountainous sites over the Chengde Experimental Area in China, we found that the clear-sky $DSR_{ins\text{-}rugged}$ over a day follows a pseudo-sine curve, depending on aspect, slope, and other terrain factors, which form the foundation of our Terrain Correction Sinusoidal Model (TCSM). TCSM also includes a new simple shadow correction method. Validation against ground measurements showed that shadow-corrected clear sky TCSM $DSR_{daily\text{-}rugged}$ estimated from in situ measurements, is highly accurate with an RMSE of 9.69 Wm^{-2}, Bias of 0.93 Wm^{-2} and R^2 of 0.99. After applying TCSM to correct the topographic effects of both the CERES SYN1deg_Ed4A and MCD18A1 C6 DSR products, the accuracies significantly improved, with the validated RMSE reduced from 63.60 and 64.51 to 14.03 and 12.60 Wm^{-2}, the Bias from -38.58 and -36.93 to 5.53 and -7.17 Wm^{-2}, and R^2 from 0.46 and 0.44 to 0.97 and 0.98, respectively. Additionally, the TCSM can be easily applied to other DSR products that do not consider the topographic effects.**

***Index Terms*—daily downward shortwave radiation, rugged terrain, clear-sky, Terrain Correction Sinusoidal Model, estimation, CERES, MCD18, remote sensing**

NOMENCLATURE

Parameter	Description
α	Daily surface broadband albedo
φ	Latitude
δ	Sun declination
θ_0	Solar zenith angle
φ_0	Solar azimuth angle
θ_i	Angles between the incident ray and the slope surface normal (solar illumination angle)
u_0	Cosine of θ_0
u_s	Cosine of θ_i
Φ	A binary function; Φ=0 if obstructed and Φ=1 if not
S	Slope
A	Aspect of slope
V_d	Sky view factor
V_c	Terrain view factor
$D_{dir\text{-}ins\text{-}flat}$	Instantaneous direct radiation at a flat surface
$D_{dif\text{-}ins\text{-}flat}$	Instantaneous diffuse radiation at a flat surface
$DSR_{ins\text{-}flat}$	Instantaneous downward shortwave radiation at a flat surface
$D_{dir\text{-}ins\text{-}rugged}$	Instantaneous direct radiation over a rugged surface
$D_{dif\text{-}ins\text{-}rugged}$	Instantaneous diffuse radiation over a rugged surface
$DSR_{ins\text{-}rugged}$	Instantaneous downward shortwave radiation over a rugged surface
$D_{ins\text{-}ref\text{-}rugged}$	Instantaneous reflected solar radiation over a rugged surface
$D_{ref\text{-}rugged}$	Reflected solar radiation from the adjacent regions

This work was funded by the National Key Research and Development Program of China (Grant No. 2020YFA0608704) and the National Natural Science Foundation of China Grants (Grant No. 42090012). *(Corresponding author: Bo Jiang).*

Hui Liang, Bo Jiang, Xiaotong Zhang, Jiakun Han, Xiuwan Yin are with the State Key Laboratory of Remote Sensing Science, Beijing Normal University and Institute of Remote Sensing and Digital Earth of Chinese Academy of Sciences, Beijing 100875, China, and Beijing Engineering Research Center for Global Land Remote Sensing Products, Faculty of Geographical Science, Institute of Remote Sensing Science and Engineering, Beijing Normal University, Beijing 100875, China, and Hui Liang is also with the School of Remote Sensing and Information Engineering, Wuhan University, Wuhan 430079, China (e-mail: huiliang@mail.bnu.edu.cn; bojiang@bnu.edu.cn; xtngzhang@bnu.edu.cn; jiakunhan@mail.bnu.edu.cn; yinxiuwan@mail.bnu.edu.cn).

Shunlin Liang is with Jockey Club STEM Laboratory of Quantitative Remote Sensing, Department of Geography, The University of Hong Kong, Hong Kong 999077, China (e-mail: shunlin@hku.hk).

Jianguang Wen is with the State Key Laboratory of Remote Sensing Science, Aerospace Information Research Institute, Chinese Academy of Sciences, Beijing 100101, China, and also with the College of Resources and Environment, University of Chinese Academy of Sciences, Beijing 100049, China (e-mail: wenjg@aircas.ac.cn).

Tao He is with Hubei Key Laboratory of Quantitative Remote Sensing of Land and Atmosphere, School of Remote Sensing and Information Engineering, Wuhan University, Wuhan 430079, China (e-mail: taohers@whu.edu.cn).

Jianghai Peng is with the Center for Global Discovery and Conservation Science, School of Earth and Space Exploration, Arizona State University, Tempe, AZ, 85281, USA (e-mail: jpeng49@asu.edu);

Shaopeng Li is with Institute of Geography and Oeschger Centre for Climate Change Research, University of Bern, CH-3012 Bern, Switzerland (e-mail: shaopeng.li@unibe.ch)

$DSR_{daily\text{-}flat}$	Daily downward shortwave radiation over a flat surface
$DSR_{daily\text{-}rugged}$	Daily downward shortwave radiation over a rugged surface
$DSR_{flat\text{-}max}$	Maximum of daily $DSR_{ins\text{-}flat}$
$DSR_{rugged\text{-}max}$	Maximum of daily $DSR_{ins\text{-}rugged}$
$t_{rugged\text{-}max}$	Time of $DSR_{rugged\text{-}max}$
$t_{flat\text{-}max}$	Time of $DSR_{flat\text{-}max}$
t_{rise}	Sunrise time
t_{set}	Sunset time
t_{us_max}	Maximum time of u_s during one day
t_{shadow}	Lasting length of the shadow during daytime
Z_d	Elevation of the adjacent pixels
Z_0	Elevation of the target pixel
d	Resolution of Digital Elevation Model (DEM)

I. INTRODUCTION

DOWNWARD shortwave radiation (DSR) with a spectral range of 0.3–3.0μm is the remaining part of solar radiation at the top of the atmosphere after it has interacted with the atmosphere [1]. As one of the most essential components of the radiative balance, DSR drives the climate system and hydrological cycle and plays an important role in various applications, such as agriculture and forest meteorology, weather forecasting, climate monitoring, and so on [1-4]. Currently, there are several remote sensing or model reanalysis products that provide accurate DSR at various tempo-spatial resolutions [5-7]. However, the estimation of DSR over rugged terrain (DSR_{rugged}), which accounts for 24% of the Earth's surface and greatly impacts DSR, is still a difficult task, especially at daily scales. Previous studies pointed out that topographic effects should be carefully considered in DSR estimation when its spatial resolution is less than 5 km [8], otherwise, the uncertainty in the estimates might be as large as 300 Wm^{-2} or exceeding 600 Wm^{-2} at instantaneous scales under clear sky [9]. For example, in the Northern hemisphere, the instantaneous DSR_{rugged} ($DSR_{ins\text{-}rugged}$) received on eastern slopes in the morning or the south-facing slopes and ridges is usually substantially larger than that on western slopes, or at canyon bottoms and north-facing slopes [10-12]. Moreover, a heightened significance of topography on DSR increases with the increase of slope [13, 14], the topographic radiative forcing (TRF) contributes 9.5% of the annual-average DSR in abrupt terrain (slopes >15°).

Under clear skies, DSR_{rugged} can be considered as consisting of direct solar radiation ($D_{dir\text{-}rugged}$), diffuse solar radiation ($D_{dif\text{-}rugged}$), and reflected radiation from the surrounding terrain ($D_{ref\text{-}rugged}$). Rugged terrain influences DSR_{rugged} by altering these three major components mainly through their slope (S), aspect (A), and shadow effects [15, 16]. Taking $D_{dir\text{-}rugged}$, which dominates DSR_{rugged}, as an example, it is determined by A and S through changes in the solar illumination angle (θ_i) [17-19], and its magnitude might be reduced shadows cast by terrain [20, 21]. Therefore, $DSR_{ins\text{-}rugged}$ is usually obtained by summing its instantaneous components: instantaneous direct radiation over a rugged surface ($D_{dir\text{-}ins\text{-}rugged}$), instantaneous diffuse radiation over a rugged surface ($D_{dif\text{-}ins\text{-}rugged}$), and instantaneous reflected solar radiation over a rugged surface ($D_{ins\text{-}ref\text{-}rugged}$) [22]. $D_{dir\text{-}ins\text{-}rugged}$ and $D_{dif\text{-}ins\text{-}rugged}$ are derived by adjusting their corresponding instantaneous direct ($D_{dir\text{-}ins\text{-}flat}$) and diffuse solar radiation over a flat surface ($D_{dif\text{-}ins\text{-}flat}$) using terrain parameters related to S, A, and shadow [23, 24], including solar zenith angle (θ_0), θ_i, sky view factors (V_d), and terrain view factors (V_c). Meanwhile, $D_{ins\text{-}ref\text{-}rugged}$ can be calculated using the average surface broadband albedo (α) of the surrounding terrain. This method, known as the direct component formula (DCF) [10, 25, 26], has been validated extensively through comparisons with ground measurements and model simulations [27] and has been widely used in previous studies[9, 26]. However, the performance of DCF heavily depends on the accuracy of the input data, especially the parameters related to atmosphere and terrain [28]. Moreover, the variations in DSR_{rugged} and how they are affected by different terrain factors have not been fully investigated.

In contrast to $DSR_{ins\text{-}rugged}$, there are relatively few studies on the more widely used daily average DSR_{rugged} ($DSR_{daily\text{-}rugged}$), even though it is greatly impacted by the interactions of S, A, and shadows [10, 15, 29]. Due to the absence of a specific method for obtaining $DSR_{daily\text{-}rugged}$, common extrapolation methods used for flat surfaces, including the direct average method and the sinusoidal model [30], which was proposed by Bisht et al. [31-33] under the assumption that solar radiation on a flat surface varies conforming a sine wave pattern throughout the day, are often directly applied to $DSR_{ins\text{-}rugged}$ to estimate $DSR_{daily\text{-}rugged}$. However, Yan et al. [10] found that the uncertainty in the $DSR_{daily\text{-}rugged}$ estimated from these methods could be as large as 60 Wm^{-2} under clear sky, particularly for the $DSR_{ins\text{-}rugged}$ obtained from the remotely sensed data with low temporal resolution (i.e., once daily) or without a noon overpass [10, 30]. Therefore, there is an urgent need for a reasonable and effective method to fully consider topographical effect to temporally extend $DSR_{ins\text{-}rugged}$ to retrieve $DSR_{daily\text{-}rugged}$.

In this study, after thoroughly analyzing DSR_{rugged} at both instantaneous and daily scales, a new model called the Topographic Correction Sinusoidal Model (TCSM) has been developed. The TCSM can characterize the theoretical variations of DSR_{rugged} on any clear day across various types of terrain. That is to say that for a specific mountain location, TCSM can easily estimate $DSR_{ins\text{-}rugged}$ and the corresponding $DSR_{daily\text{-}rugged}$ under clear sky conditions using in situ measurements or remotely sensed data providing the needed instantaneous DSR-related parameters. The performance of TCSM has been fully evaluated against ground measurements using different data sources as inputs. Note that only clear-sky condition was discussed in this study. The remainder of this paper is organized as follows: Section 2 introduces the data and their pre-processing, Section 3 provides an overview of TCSM, Section 4 presents the evaluation results of TCSM, and Section 5 delivers the discussions and conclusions.

II. Data and Pre-processing

This study used ground measurements and remotely sensed data. The ground measurements were collected from seven sites over rugged terrain. The remotely sensed data included Clouds and Earth's Radiant Energy Systems synoptic Edition4 (CERES-SYN1deg_Ed4A, hereinafter CERES4) and MCD18A1 C6 (MCD18 for short), which provide direct, diffuse solar radiation and DSR, Shuttle Radar Topography Mission Digital Elevation Model (SRTM DEM) data, and the Global LAnd Surface Satellite (GLASS) broadband albedo product. More details are introduced below.

A. Ground measurements

The DSR ground measurements were from seven sites over the Chengde Experimental Area (42.3°N−42.5°N, 117.3°E−117.5°E), located in the Saihanba Forest Park of Chengde, Moon Mountain, on the eastern margin of the Xiaoluanhe River Basin, northeastern China (Fig. 1). This region has a distinct topographic relief, with elevations ranging between 1272–1654 m and most slopes around 30°. Its major land cover is grassland and the slope is uniform, which facilitates the installation and maintenance of ground measurement sites.

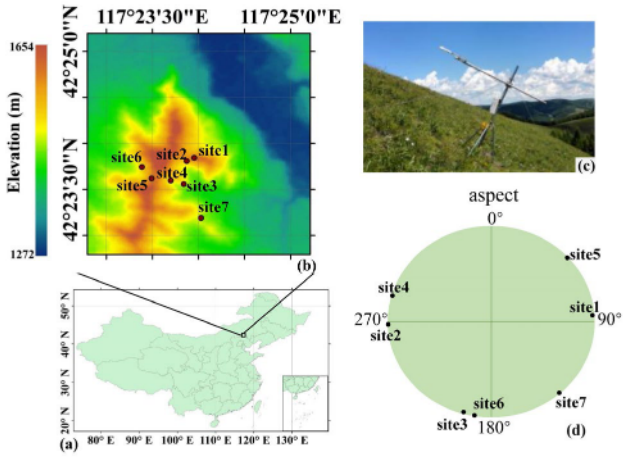

Fig. 1. (a-b) Geographic location and elevation of the study region, and spatial distribution of the seven sites (site1–7); (c) the radiometer is set parallel to the inclined surface; (d) the aspect of each site.

Detailed information about the sites is listed in Table I. The seven sites are situated in proximity to each other, predominantly mostly on medium slopes (20° − 30°), except for sites 5 and 1, but at different aspects (Fig. 1d). EKO or CNR4 radiometers were installed at all sites at a height of ~1.5m to measure solar radiation at one-minute intervals [10, 27, 34]. The instruments were mounted parallel to the slope of the terrain (Fig. 1c) as this is considered necessary to measure the DSR over rugged terrain [10]. Eq. (1) is the mathematical expression of θ_i (in degrees from the normal to the terrain):

$$u_s = \cos\theta_i = u_0 \times \cos\mathrm{S} + \sin\theta_0 \times \sin S \times \cos(\varphi_0 - \mathrm{A}) \quad (1)$$

$$u_0 = \cos\theta_0 \quad (1a)$$

where φ_0 (in degrees from north) is the solar azimuth angle and θ_0 (in degrees from the vertical direction) is the solar zenith angle, which were both calculated from the Solar Position Calculator [35]. Note that the measurements at site7 were of suboptimal quality due to the inclination of the measuring instrument, which was prone to tilting because of the steep slope.

TABLE I
Detailed Information about the Seven Sites in the Chengde Experimental Area

Site No.	Latitude (°)	Longitude (°)	Elevation (m)	*S* (°)	*A* (°)
site1	42.397	117.399	1848.551	9	85
site2	42.397	117.398	1848.427	19	269
site3	42.393	117.397	1852.700	26	196
site4	42.393	117.395	1810.066	22	285
site5	42.394	117.392	1700.166	2	47
site6	42.396	117.390	1756.811	29	189
site7	42.387	117.400	1838.169	30	138

All radiative measurements in the Chengde Experimental Area were strictly quality-controlled by removing all unreasonable outliers and are therefore deemed of good quality. These measurements have been successfully applied in other studies [26, 36]. This study used only the quality-controlled DSR observations at sites 1−7 from 2018 to 2019 recorded during clear-sky conditions. For convenience, a half-hour was defined as the instantaneous scale, following Ma et al. [26]. Hence, all screened 1-minute measurements were first aggregated into half-hour averages, centered on each half-hour during the daytime, with no missing data allowed. Subsequently, these half-hour averages were aggregated into daily averages, again without any missing data. Finally, a total of 228 daily samples for clear days were obtained for independent validation.

B. Remotely sensed data

1) Satellite product providing $D_{dir\text{-}ins\text{-}flat}$, $D_{dif\text{-}ins\text{-}flat}$, and $DSR_{ins\text{-}flat}$

a) CERES4

Studies have shown that the DSR from CERES-SYN1deg_Ed4A published by the National Aeronautics and Space Administration (NASA; https://ceres.larc.nasa.gov, last accessed 23/Aug/2024) is one of the most accurate global radiative products [37-39]. Its radiative components, including $D_{dir\text{-}ins\text{-}flat}$, $D_{dif\text{-}ins\text{-}flat}$, and instantaneous downward shortwave radiation at flat surface ($DSR_{ins\text{-}flat}$), are calculated using the Langley Fu-Liou radiative transfer model. This model calculates radiative transfer without considering topographic effects and incorporates cloud and aerosol parameters derived from the Moderate Resolution Imaging Spectroradiometer (MODIS), geostationary satellites (GEO), and the Global Modeling and Assimilation Office (GMAO) [40] at a spatial size of 1° and at hourly intervals from 2000 onward. In this study, CERES4 was first resampled into a half-hour resolution, after which the corresponding CERES4 $D_{dir\text{-}ins\text{-}flat}$, $D_{dif\text{-}ins\text{-}flat}$, and $DSR_{ins\text{-}flat}$ in 2018 and 2019 were extracted at local times

for the six mountainous sites. Site 5, which was located on a flat surface, was excluded from this process.

b) MCD18

The MCD18A1 C6 product, released by NASA (https://lpdaac.usgs.gov/, last accessed 23/Aug/2024), was generated using the look-up-table (LUT) method. This method uses top-of-atmosphere reflectance from MODIS and auxiliary data, including geographic locations, surface albedo from MCD43A3, vapor pressure from Modern-era Retrospective Analysis for Research and Applications, Version 2 (MERRA2), elevation from the Global 30 Arc-Second Elevation data set (GTOPO30), and surface reflectance climatology data [37]. Compared to CERES4, MCD18 only provides $D_{dir\text{-}ins\text{-}flat}$, $D_{dif\text{-}ins\text{-}flat}$, and $DSR_{ins\text{-}flat}$ at satellite overpass time, in addition to providing $DSR_{ins\text{-}flat}$ every three hours at a spatial resolution of 5 km. In this study, the $D_{dir\text{-}ins\text{-}flat}$, $D_{dif\text{-}ins\text{-}flat}$, and $DSR_{ins\text{-}flat}$ corresponding to the overpass times of MCD18 were extracted at six of the sites (excluding site 5). Moreover, the three-hourly $DSR_{ins\text{-}flat}$ were also extracted to be used for evaluation purposes. All data were converted to local time.

2) GLASS broadband albedo product

The GLASS surface broadband albedo product (http://glass.umd.edu/, last accessed 23/Aug/2024) is derived directly from MODIS and the Advanced Very High-Resolution Radiometer (AVHRR) satellite reflectance data using the LUT method. The LUT was established using site measurements and model simulations covering a range of regions, types of land cover, and seasons on a global scale [41-43]. Its high accuracy was confirmed through validation with the MODIS surface albedo product [42, 44, 45] and other model simulation products [46]. In this study, albedo α at a spatial resolution of 250 m and a temporal resolution of four days in 2018 and 2019 was extracted to match the ground measurements. The values of α were considered constant within each four-day period by assuming that the variations in albedo could be neglected during these intervals. Furthermore, it was assumed that the α of a point was the same as the averaged α of the surrounding terrain, defined within a 3×3 window, following Ma et al. [26].

3) SRTM DEM

The DEM from SRTM (https://lpdaac.usgs.gov/, last accessed 23/Aug/2024) was generated by NASA, the National Geospatial-Intelligence Agency (NGA), and the German and Italian space agencies. Generated using radar interferometry, it covers about 80% of the global land surface between 60°N and 56°S. It has the WGS84 coordinate system and a spatial resolution of 1 rad/s (~30 meters) [47]. According to Tang et al. [48], SRTM is the most accurate global digital elevation dataset available. In this study, we assumed that each pixel represented a single slope surface [49, 50], and used the DEM to calculate S, A, V_d, V_c and whether the target pixel was sheltered by neighboring pixels or not. Fig. 2 shows an example where the topographic factors of the target pixel Z_5 are determined using the terrain information of the adjacent pixels in a 3×3 window, according to Wu et al. [22] applying Eq. (2).

Z_1	Z_2	Z_3
Z_4	Z_5	Z_6
Z_7	Z_8	Z_9

Fig. 2. $Z_1 - Z_9$ represent the elevations corresponding to each pixel.

$$f_x = \frac{Z_8 - Z_2}{2 \times d}, f_y = \frac{Z_6 - Z_4}{2 \times d} \tag{2}$$

$$S = \arctan\sqrt{f_x^2 + f_y^2} \tag{2a}$$

$$A = 270° + \arctan(\frac{f_y}{f_x}) - 90° \frac{f_y}{|f_x|} \tag{2b}$$

$$V_d = \frac{(1 + \cos S)}{2} \tag{2c}$$

$$V_c = 1 - V_d \tag{2d}$$

where d is the spatial resolution of 30 m of the SRTM DEM data.

In this study, the effect of shadows was also considered. An evaluation method proposed by Giles et al. [51] was used to determine whether a pixel was a shadow caused by adjacent terrain. The method is given in Eq. (3), and the adjacent region was defined as a 3×3 pixel window, as suggested by Wu et al. [22] and Zhou et al. [52]. As shown in Eq. (3), if the elevation of any pixel in the adjacent region (Z_d) of the target point is greater than the threshold elevation when it is just sheltered (h) of the target point, then the target point would be considered to be shadowed:

$$Z_d \geq h = Z_0 + d \times \tan(90 - \theta_0) \tag{3}$$

where Z_0 is the elevation of the target pixel.

III. Methodology

A. TCSM introduction

1) Mathematical expression of TCSM

After careful analysis, we found that the maximum of daily $DSR_{ins\text{-}rugged}$ ($DSR_{rugged\text{-}max}$) and the corresponding time of $DSR_{rugged\text{-}max}$ ($t_{rugged\text{-}max}$) are crucial for determining the variations of $DSR_{ins\text{-}rugged}$. Specifically, $DSR_{rugged\text{-}max}$ is affected by the combined effects of various factors, particularly S and A, in line with findings from previous studies [9, 29, 50, 53], while $t_{rugged\text{-}max}$ is primarily determined by A. Fig. 3 shows the schematic diagram for the DSR variations of a specific point on a clear day. If the point is on a flat surface, then its $DSR_{ins\text{-}flat}$ varies conforming to a sinusoidal curve, peaking at the time of maximum of daily $DSR_{ins\text{-}flat}$ ($t_{flat\text{-}max}$) of ~12:30hrs [31-33], as indicated by the black line in Fig. 3. If the point is on a due south (A=180°) or due north slope (A=0°/360°), then the shape of its $DSR_{ins\text{-}rugged}$ throughout that day would remain unchanged except for the magnitude of $DSR_{rugged\text{-}max}$, as depicted by the pink lines a or b. Hence, the $DSR_{ins\text{-}rugged}$ can be expressed by Eq. (4) as the sinusoidal curve.

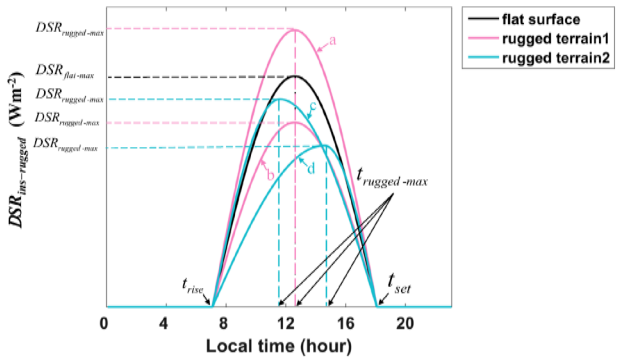

Fig. 3. Schematic diagram of the variation of clear-sky DSR_{rugged} curves (pink and blue lines) compared to the one from a flat surface (black line). The pink curves *a* and *b* show the variations of the DSR_{rugged} on the south and the north slopes, respectively, and the blue curves *c* and *d* show the variations of the DSR_{rugged} on the east and west slopes, respectively. The corresponding colored vertical dash lines indicate the maximum of DSR and its time.

However, if the point is on the eastern slope ($A \in (0°,180°)$) or western slope ($A \in (180°, 360°)$), then the $DSR_{rugged\text{-}max}$ and $t_{rugged\text{-}max}$ both would change, with the $t_{rugged\text{-}max}$ before or after $t_{flat\text{-}max}$ (12:30hrs) respectively, as the blue lines *c* or *d* shown in Fig. 3. In this case, the variations of $DSR_{ins\text{-}rugged}$ could be regarded as the pseudo sine curve adjusted from the sine curve (black line) by altering the location and magnitude of its peak. Thereby, the pseudo sine curve consists of two sine segments with the same peak of $DSR_{rugged\text{-}max}$ and $t_{rugged\text{-}max}$ acting as the cut-off point, with one segment extending from the sunrise time (t_{rise}) to $t_{rugged\text{-}max}$ and the other one from $t_{rugged\text{-}max}$ to sunset time (t_{set}), mathematically expressed as Eq. (5) modified from Eq.(4).

when $A = 0°(360°)/180°$,

$$DSR_{rugged}(t) = DSR_{rugged\text{-}max} \times \sin[(\frac{t - t_{rise}}{t_{set} - t_{rise}})\pi], \tag{4}$$

when $A \in (0°,180°) \cup (180°,360°)$,

$$DSR_{rugged}(t) = \begin{cases} DSR_{rugged\text{-}max} \times \sin[(\frac{t - t_{rise}}{(t_{rugged\text{-}max} - t_{rise}) \times 2})\pi], \\ t \le t_{rugged-max} \\ DSR_{rugged\text{-}max} \times \sin[(\frac{t_{set} - t}{(t_{set} - t_{rugged\text{-}max}) \times 2})\pi], \\ t > t_{rugged-max} \end{cases} \tag{5}$$

where t_{rise} and t_{set} could be calculated as:

$$t_{rise} = 12 - \frac{1}{15} \times \arccos[-\tan(\varphi) \times \tan(\delta)] \tag{6}$$

$$t_{set} = 12 + \frac{1}{15} \times \arccos[-\tan(\varphi) \times \tan(\delta)] \tag{7}$$

where φ is the latitude (in radians), and δ is the solar declination (in radians).

Therefore, the combination of Eqs. (4) and (5) is called TCSM, and it can be used to simulate DSR_{rugged} at any moment and place during daytime under clear-sky conditions. Accordingly, the corresponding $DSR_{daily\text{-}rugged}$ could be calculated by averaging the integration of $DSR_{ins\text{-}rugged}$ during t_{rise} and t_{set} over 24 hours, as Eqs. (8) and (9), respectively:

when $A = 0°(360°)/180°$,

$$\begin{aligned} DSR_{daily-rugged} &= \frac{\int_{t_{rise}}^{t_{set}} DSR_{rugged}(t)\,\mathrm{d}t}{24} \\ &= \frac{DSR_{rugged\text{-}max}}{12\pi} \times (t_{set} - t_{rise}), \end{aligned} \tag{8}$$

when $A \in (0°,180°) \cup (180°,360°)$,

$$\begin{aligned} DSR_{daily-rugged} &= \frac{\int_{t_{rise}}^{t_{rugged-max}} DSR_{rugged}(t)\,\mathrm{d}t}{24} + \frac{\int_{t_{rugged-max}}^{t_{set}} DSR_{rugged}(t)\,\mathrm{d}t}{24} \\ &= \frac{DSR_{rugged\text{-}max}}{12\pi} \times (t_{rugged\text{-}max} - t_{rise}) \\ &\quad + \frac{DSR_{rugged\text{-}max}}{12\pi} \times (t_{set} - t_{rugged\text{-}max}) \\ &= \frac{DSR_{rugged\text{-}max}}{12\pi} \times (t_{set} - t_{rise}), \end{aligned} \tag{9}$$

From the two equations, it can be seen that the calculation of the clear-day $DSR_{daily\text{-}rugged}$ for any place with a known A only depending on $DSR_{rugged\text{-}max}$. In this study, as long as $t_{rugged\text{-}max}$ was determined, $DSR_{rugged\text{-}max}$ could be obtained from ground measurements or calculated from the DSR satellite products. More details about the determination of $t_{rugged\text{-}max}$ and $DSR_{rugged\text{-}max}$ are introduced below.

2) Determination of $t_{rugged\text{-}max}$ and $DSR_{rugged\text{-}max}$ in TCSM

a) t_{rugged_max}

In order to obtain $t_{rugged\text{-}max}$, the change in the $t_{rugged\text{-}max}$ from the $t_{flat\text{-}max}$ (~12:30hrs) for different A was examined firstly and the results shown in Fig. 4. As Fig. 4 shows, $t_{rugged\text{-}max}$ is the same as $t_{flat\text{-}max}$ if A=0º (360º) or180º. When A increases from 0° to 180°, $t_{rugged\text{-}max}$ moves forward to t_{rise} and then moves backward to $t_{flat\text{-}max}$ with the earliest $t_{rugged\text{-}max}$ appearing at A=90º; whereas when A increases from 180° to 360°, $t_{rugged\text{-}max}$ moves forward to t_{set} and then moves backward to $t_{flat\text{-}max}$ with the latest $t_{rugged\text{-}max}$ appearing at A=270º. Theoretical, $t_{rugged\text{-}max}$ with different A could be deduced from $t_{flat\text{-}max}$.

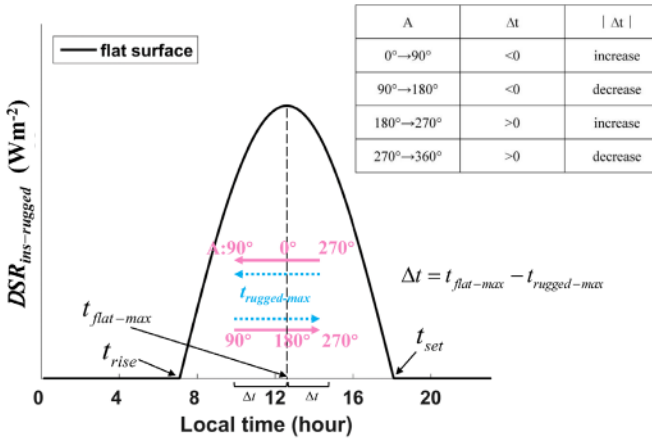

A	Δt	| Δt |
0°→90°	<0	increase
90°→180°	<0	decrease
180°→270°	>0	increase
270°→360°	>0	decrease

Fig. 4. Schematic diagram illustrating the changes of $t_{rugged\text{-}max}$ with A by referring to $t_{flat\text{-}max}$ (12:30 hrs) of the DSR sinusoidal curve on a flat surface. Δt represents the difference between $t_{flat\text{-}max}$ and $t_{rugged\text{-}max}$.

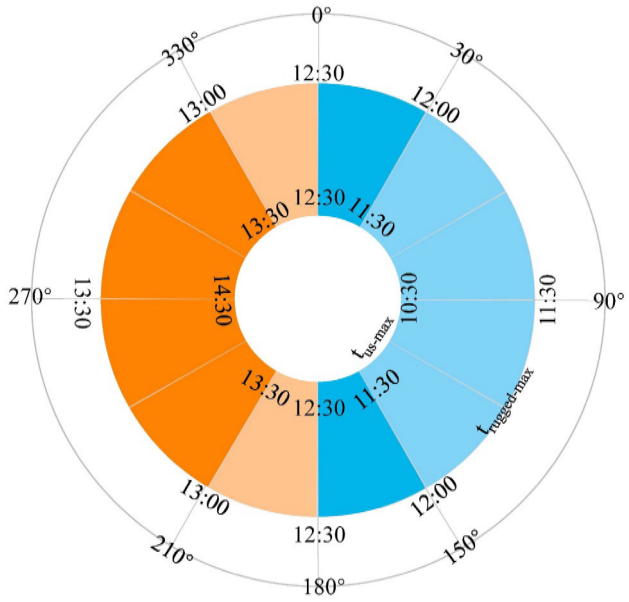

Fig. 5. Variations of $t_{us\text{-}max}$ (the inner colored circle) and $t_{rugged\text{-}max}$ (the outer colored circle) with A (the outermost circle). Blue indicates that $t_{rugged\text{-}max}$ is before 12:30hrs, and vice versa for orange color.

However, in this study, due to the very limited available ground measurements, the determination of t_{rugged_max} could only be referred to the time of the maximum u_s (t_{us_max}) by considering the close relationship between DSR_{rugged} and u_s [9], and t_{us_max} can be easily retrieved from Eq. (1). By setting different values of S ($S \in (0°, 90°)$ at 1° intervals), A ($A \in [0°, 360°)$ at 1° intervals), day of year (DOY $\in [1, 365]$ at daily time steps), and half hour time steps, the comprehensive u_s samples were calculated from Eq. (1), and then the variations in t_{us_max} were explored. Note that the φ_0 and θ_0 in Eq. (1) were calculated from DOY and the specific moment. Our analysis found that t_{us_max} is mainly influenced by A, and the t_{us_max} is equal to 12:30hrs, 10:30hrs, 12:30hrs, and 14:30hrs for A is 0°, 90°, 180°, and 270°, respectively. The variations in t_{us_max} with A is illustrated as the inner color circle in Fig. 5, in which the outmost circle represents A.

Afterwards, the "true" t_{rugged_max} from the six mountainous sites were inter-compared with the corresponding simulated t_{us_max}. For site1 (A=85°) and site2 (A=269°), which were near the due east and west slopes, their averaged t_{rugged_max} were ~11:30hrs and ~13:30hrs, respectively, and t_{rugged_max} was 12:30hrs at A=0°(360°)/180° as described above. Hence, if A increases from 90° to 180° and then 270°, then t_{us_max} changes four hours in total from 10:30hrs to 12:30hrs and then 14:30hrs (inner colored circle in Fig. 5), but the corresponding t_{rugged_max} changes only about two hours in total from 11:30hrs to 12:30hrs and then 13:30hrs (outer colored circle in Fig. 5). Therefore, it is reasonable to assume that t_{rugged_max} varies with A similarly to t_{us_max} but in the ratio of 1:2. Accordingly, t_{rugged_max} was speculated to be 12:00hrs for A=30°/150° and 13:00hrs for A=210°/330°. Overall, due to the rugged terrain, u_s varied differently compared to $DSR_{ins\text{-}rugged}$, which means t_{rugged_max} is not the same as t_{us_max}, except when A is 0°(360°) or 180°. t_{rugged_max} is later than t_{us_max} when $A \in (0°, 180°)$ and vice versa when $A \in (180°, 360°)$. Note that the t_{rugged_max} from measurements represents an average value, with a typical range of plus or minus half an hour.

Combining the inner and outer colored circles, t_{rugged_max} decreases half hour per 30° of A for $A \in [0°, 30°] \cup [150°, 180°]$ and half hour per 60° of A for $A \in [30°, 150°]$ (blue in Fig. 5), whereas t_{rugged_max} would increase half hour per 30° of A for $A \in [180°, 210°] \cup [330°, 360°]$ and half hour per 60° of A for $A \in [210°, 330°]$ (orange in Fig. 5). Hence, A from 0~360° is divided into eight bins (A=0°, 30°, 90°, 150°, 180°, 210°, 270°, and 330°), and the corresponding theoretical averaged t_{rugged_max} for all slopes in these bins are 12:30hrs, 12:00hrs, 11:30hrs, 12:00hrs, 12:30hrs, 13:00hrs, 13:30hrs, 13:00hrs, respectively. Thus, for any values of A, its averaged t_{rugged_max} is determined by the bin it belongs to, and it is suggested to select the moment whose A is the closest to. But for those aspects near the median value of one bin, it is suggested to take the moment whose A is close to 0° (360°) or 180° as their averaged $t_{rugged\text{-}max}$. For example, the A of site6 was 189°, thus belonging to bin [180°, 210°]; so, its averaged t_{rugged_max} should be 12:30hrs as 189° was closer to 180° than 210°; while the A of site3 was 196°, which was in the middle of bin [180°, 210°]; so, its averaged $t_{rugged\text{-}max}$ was determined as 12:30hrs. Similarly, the obtained averaged $t_{rugged\text{-}max}$ for site2 (A=269°) was 13:30hrs, for site4 (A=285°) was 13:30hrs, and for site7 (A=138°) was 12:00hrs. They all matched well with those obtained from the measurements basically. After validation, we found that the uncertainty of the TCSM $DSR_{daily\text{-}rugged}$ estimates resulted from the determination of t_{rugged_ma} from Fig.5 (within 30min) was negligible.

b) $DSR_{rugged\text{-}max}$

With the known $t_{rugged\text{-}max}$, the corresponding $DSR_{rugged\text{-}max}$ could be extracted from the measurements or calculated from the products providing the $D_{dir\text{-}ins\text{-}flat}$, $D_{dif\text{-}ins\text{-}flat}$, and $DSR_{ins\text{-}flat}$ at flat surface with DCF method [10, 25, 26] . Note that the three

DSR related parameters were assumed the same in one pixel for any products.

$$\begin{aligned} DSR_{ins-rugged} &= D_{dir-ins-rugged} + D_{dif-ins-rugged} + D_{ins-ref-rugged} \\ &= D_{dir-ins-flat} \times (u_s / u_0) \times \Phi + D_{dif-ins-flat} \times V_d \\ &\quad + V_c \times \alpha \times DSR_{ins-flat} \end{aligned} \tag{10}$$

where $D_{dir\text{-}ins\text{-}rugged}$ (Wm^{-2}) and $D_{dif\text{-}ins\text{-}rugged}$ (Wm^{-2}) are the instantaneous direct and diffuse solar radiation over rugged terrain for a given point, $D_{ins\text{-}ref\text{-}rugged}$ (Wm^{-2}) is the reflected solar radiation from the adjacent region (within a 3×3 window); α was obtained from the GLASS broadband albedo product, and Φ represents the binary shadow function, with a value of 1 or 0, indicating whether the pixel receives direct radiation (determined by Eq. (3)) or not.

If the available measurements or products (i.e., CERES4) are temporal continuous, then the most convenient way is to resample them into a half-hour scale, so the in-situ $DSR_{rugged\text{-}max}$ could be obtained directly from the measurements or calculated from the products at the exact moment of $t_{rugged\text{-}max}$. However, if the measurements or products are only available at times different than $t_{rugged\text{-}max}$, such as the $D_{dir\text{-}ins\text{-}flat}$, $D_{dif\text{-}ins\text{-}flat}$, and $DSR_{ins\text{-}flat}$ provided by MCD18 only at the satellite overpass time ($t_{overpass}$) (see Fig. 6), then the $DSR_{rugged\text{-}max}$ should be retrieved by interpolation.

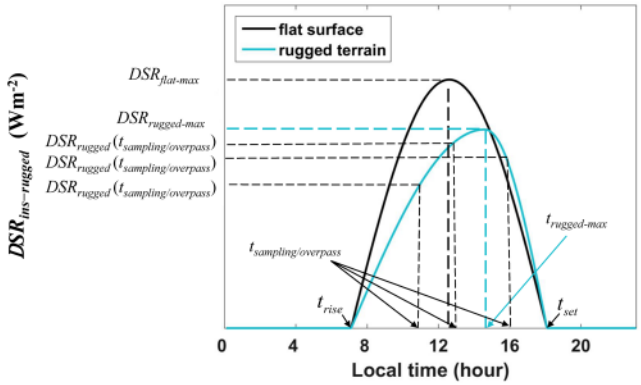

Fig. 6. Schematic diagram of DSR_{rugged} at the satellite overpass time.

As shown in Fig. 6, the measurement sampling moment ($t_{sampling}$) or $t_{overpass}$ ($t_{sampling/overpass}$) might be before or after $t_{rugged\text{-}max}$. In this case, the $DSR_{rugged\text{-}max}$ could be calculated through the DSR_{rugged} from measurement at $t_{sampling}$ or calculated from the product at $t_{overpass}$ ($DSR_{rugged}(t_{samping/overpass})$) according to Eq. (11). Note that the $DSR_{rugged}(t_{sampling/overpass})$ for products should be computed at first using DCF (Eq. (10)).

$$\begin{aligned} &if \quad t_{sampling/overpass} \le t_{rugged\text{-}max}, \\ &DSR_{rugged\text{-}max} = \frac{DSR_{rugged}(t_{sampling/overpass})}{\sin[(\frac{t_{sampling/overpass} - t_{rise}}{(t_{rugged\text{-}max} - t_{rise}) \times 2})\pi]} \\ &if \quad t_{sampling/overpass} > t_{rugged\text{-}max}, \\ &DSR_{rugged\text{-}max} = \frac{DSR_{rugged}(t_{sampling/overpass})}{\sin[(\frac{t_{set} - t_{sampling/overpass}}{(t_{set} - t_{rugged\text{-}max}) \times 2})\pi]} \end{aligned} \tag{11}$$

If more than one $DSR_{rugged}(t_{samping/overpass})$ was available in one day, then the maximum $DSR_{rugged\text{-}max}$ was suggested to be used for the $DSR_{daily\text{-}rugged}$ calculation. Besides, the interpolation method could also be applied to the temporal continuous measurements or products without resampling. However, it was found that the $DSR_{rugged\text{-}max}$ obtained from the two methods would affect the $DSR_{daily\text{-}rugged}$ estimation accuracy. More related discussions are provided in Section IV *B*. 2).

3) Shadow correction

The influence of the self-shadow (u_s<0) and the shadow cast by the adjacent terrain on $DSR_{daily\text{-}rugged}$ is also taken into account in this study. From measurements, it was found that the shadow usually appears for a short period after sunrise and/or before sunset, but its occurrence time and duration are different over different kinds of terrain. Hence, the duration of the shadow (t_{shadow}) could be estimated as long as the t_{rise}, t_{set}, and the time for u_s=0 ($t_{u_s=0}$) are known. If $t_{u_s=0}$ is in the morning (afternoon), then t_{shadow} (unit: h) is the period between $t_{u_s=0}$ and t_{rise} (t_{set}).

Based on in situ samples with shadows (No. of samples=154), their shadow occurrence time, t_{shadow}, and the residual $\Delta DSR_{daily\text{-}rugged}$ which was calculated by minus the observations from their TCSM $DSR_{daily\text{-}rugged}$ estimates were obtained, respectively. Afterwards, the scatter plot between the $\Delta DSR_{daily\text{-}rugged}$and the t_{shadow} for different shadow occurrence time is shown in Fig. 7. $\Delta DSR_{daily\text{-}rugged}$ were mostly positive and increased with t_{shadow} (≤5h) when the shadow appeared at sunrise (red dots), and vice versa at sunset (black dots). Whereas the number of samples with shadows that appeared at both sunrise and sunset (green dots) was higher, the $\Delta DSR_{daily\text{-}rugged}$ also negatively related to t_{shadow} (≤1.5h).

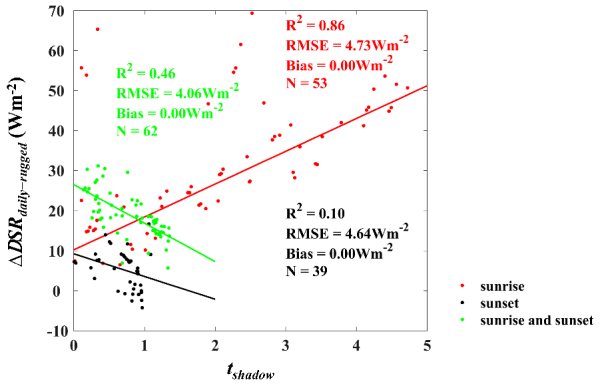

Fig. 7. Relationship between the $\Delta DSR_{daily\text{-}rugged}$ (minus the corresponding measurements from the TCSM $DSR_{daily\text{-}rugged}$ estimates) and the t_{shadow} in three cases: sunrise, sunset, and both.

Hence, the relationship between $\Delta DSR_{daily\text{-}rugged}$ and t_{shadow} can be roughly divided into three cases, including shadows occurring at sunrise, sunset, and both, and modelled separately using the following linear regression method:

$$\Delta DSR_{daily-rugged} = \begin{cases} -3.618 \times t_{shadow} + 6.407, & sunset \\ 7.680 \times t_{shadow} + 8.512, & sunrise \\ -10.517 \times t_{shadow} + 23.235, & sunrise\ and\ sunset \end{cases} \tag{12}$$

Therefore, Eq. (12) is the shadow correction model to correct the TCSM $DSR_{daily\text{-}rugged}$ estimates as long as the t_{shadow} was larger than 0. However, any findings have not been obtained about the $DSR_{ins\text{-}rugged}$ influenced by shadow, so the TCSM $DSR_{ins\text{-}rugged}$ estimates should be used with more cautions when shadow appeared.

B. Model Performance Evaluation

The performance of TCSM in simulating $DSR_{ins\text{-}rugged}$ and estimating $DSR_{daily\text{-}rugged}$ was evaluated against ground measurements. Specifically, the accuracy of the TCSM $DSR_{daily\text{-}rugged}$ estimated by taking the inputs from measurements and two remotely sensed products, including CERES4 and MCD18, was validated. Three statistical measures were used to characterize the validation accuracy: root mean square error (RMSE), Bias, and coefficient of determination (R^2).

$$Bias = \frac{\sum_{i=1}^{N}(Y_i - X_i)}{N} \tag{13}$$

$$RMSE = \sqrt{\frac{1}{N}\sum_{i=1}^{N}(X_i - Y_i)^2} \tag{14}$$

$$R^2 = 1 - \frac{\sum_{i=1}^{N}(X_i - Y_i)^2}{\sum_{i=1}^{N}(X_i - \overline{X})^2} \tag{15}$$

where Y_i and X_i are the estimate and the measurement, and N represents the number of samples.

IV. Results and Analysis

A. TCSM $DSR_{ins\text{-}rugged}$ Simulations under Clear-sky

First of all, the changes of the two crucial parameters $DSR_{rugged\text{-}max}$ and $t_{rugged\text{-}max}$ in TCSM from those at a flat surface were examined using ground measurements. According to Liang et al. [14], the topographical effects on DSR could be negligible when S<10°, hence the DSR measurements at site5 (S=2°, Table I) could be taken as the one at flat surface and served as a reference for other mountainous sites (sites1–4 and site6) in Chengde Experimental area because of their close spatial distribution. Taken the variations of the $DSR_{ins\text{-}rugged}$ on the 259th day of 2018 at sites 1−4 and 6 as examples shown in Fig. 8a–e in colored lines, and the site5 DSR curve on the same day was added in each plot in a black line for comparison. Meanwhile, the corresponding u_s of these sites is also shown with the colored dashed line in these plots. Note that the red circles indicate the periods influenced by shadows.

Fig. 8 shows that site5 DSR varies conforming to a nearly theoretical sinusoidal curve, with its maximum value ($DSR_{flat\text{-}max}$) appearing around 12:30 hrs. The times of t_{rise} and t_{set} are nearly the same as those of the other five sites, which further confirms the little topographic effects at site5 and justifies using its DSR as the reference for other sites. From this figure, the changes of $t_{rugged\text{-}max}$ at these sites were coincident very well with Fig.5. Specifically, the $t_{rugged\text{-}max}$ was nearly one hour before 12:30hrs for site1 (A=85°) (Fig. 8a), but nearly more than one hour after 12:30hrs for site2 (A=269°) and site4 (A=285°) (Fig. 8b and d); while it was nearly unchanged for site3 (A=196°) and site6 (A=189°) near the southern slope (Fig. 8c and e). Meanwhile, the time for t_{us_max} (the intersection of the vertical dashed color line and x-axis in Fig. 8) was different with $t_{rugged\text{-}max}$, and their relation were generally matched that in Fig.5. For $DSR_{rugged\text{-}max}$, the values were slightly smaller than the $DSR_{flat\text{-}max}$ for sites1, 2, and 4, but were higher by 190−260 Wm^{-2} at sites3 and 6 on the southern slope, which was possibly due to the longer exposure during the daytime on the sunny slope [54]. This supports the commonly observed underestimation of radiative components over rugged terrain, especially on sunny slopes [55, 56]. Additionally, $DSR_{rugged\text{-}max}$ at site4 (S=22°) was smaller than that of site2 (S=19°), despite having similar aspects, indicating that the influence of S on $DSR_{rugged\text{-}max}$ also exists. Hence, the descriptions on $DSR_{rugged\text{-}max}$ and $t_{rugged\text{-}max}$ in TCSM agreed well with the observations.

Afterwards, the variations in DSR_{rugged} across some clear days for sites 1–4 and 6–7 were simulated using TCSM by taking the corresponding $DSR_{rugged\text{-}max}$ measurements as the inputs and are presented in Fig. 9a−f. The corresponding in situ measurements were added to each plot for comparison in color dashed lines.

Overall, the TCSM $DSR_{ins\text{-}rugged}$ simulations under clear sky without shadow captured the variations of the measurements at all sites very well, but the overestimations were observed for some days in the periods near t_{rise} and t_{set}. Specifically, the $DSR_{ins\text{-}rugged}$ was overestimated more significantly at the sites on the western slope, such as sites2 and 4 (Fig. 9b and d), while the least overestimation appeared at site6 (Fig. 9e) and 3 (Fig. 9c), which are close to the due south slope. This is consistent with the study of Yan et al. [10] , which found that the closer to the south slope the smaller topographic effect on DSR. By combining with Fig. 8, the overestimation in the $DSR_{ins\text{-}rugged}$ was mostly because of the shadows, which has not been considered in TCSM at instantaneous scale. However, the overestimation occurred at site7 (Fig. 9f) was mostly due to the poor quality of the measurements.

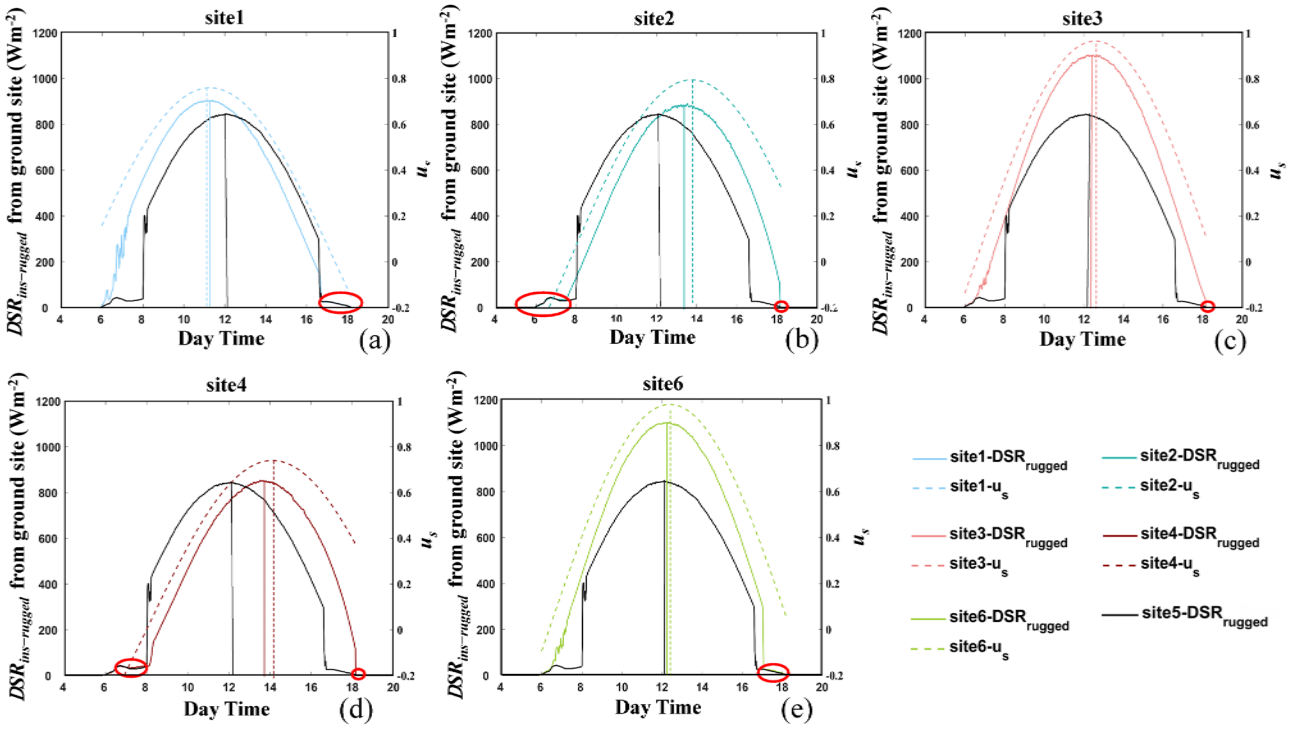

Fig. 8. DSR measurements and corresponding u_s (cosine of the solar illumination angle, see Eq. (1)) during the daytime on the 259th day of 2018 at (a-d) sites 1 − 4 and (e) site 6. The DSR at site 5 is taken as the reference shown in each plot in black line, and the red circles indicate the periods during which the site was shadowed. The intersection of the vertical lines with the curves (x-axis) presents the maximum values of the DSR or the corresponding u_s (the corresponding times).

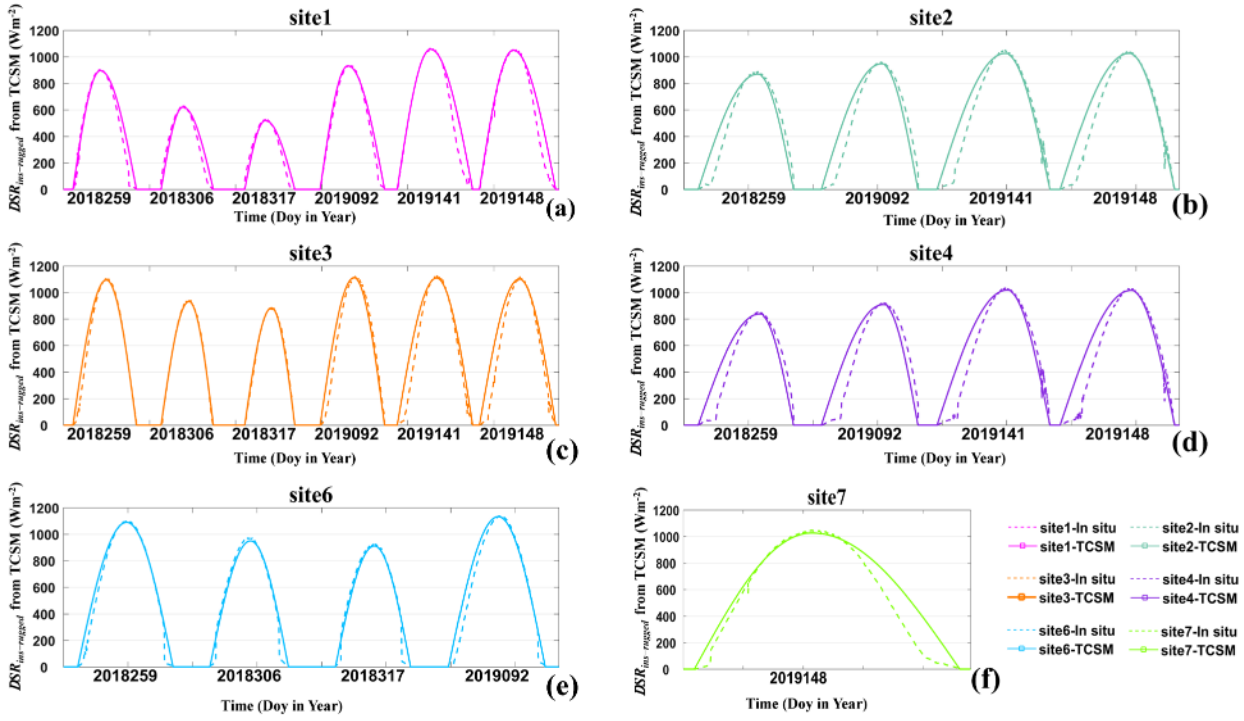

Fig. 9. DSR_{rugged} simulations from TCSM at the six mountainous sites (sites 1–4 and sites 6–7) on several clear days: (a) the 259th, 306th, 317th in 2018, and the 92nd, 141st, 148th in 2019 at site 1, (b) the 259th in 2018, and the 92nd, 141st, 148th in 2019 for site 2, (c) the 259th, 306th, 317th in 2018, and the 92nd, 141st, 148th in 2019 for site 3, (d) the 259th in 2018, and the 92nd, 141st, 148th in 2019 for site 4, (e) the 259th, 306th, 317th in 2018, and the 92nd in 2019 for site 6, and (d) the148th in 2019 for site 7. Note that the dates shown on the x-axis are non-continuous.

B. TCSM $DSR_{daily\text{-}rugged}$ estimation validation accuracy

As described above, $t_{rugged\text{-}max}$ could be easily determined by A according to Fig. 5, and then the corresponding $DSR_{rugged\text{-}max}$, which is needed for calculating $DSR_{daily\text{-}rugged}$ with Eqs. (8) and (9), could be derived from measurements or products with the calculated t_{rise} and t_{set}. In addition, the $DSR_{daily\text{-}rugged}$, estimated from the Sinusoidal model by taking the measurements as inputs, were also validated for comparison. Note that only clear sky conditions were considered in this study.

1) $DSR_{rugged\text{-}max}$ from measurements

The scatter plot between the TCSM $DSR_{daily\text{-}rugged}$ estimates and the ground measurements is shown in Fig. 10. Overall, the estimates agreed well with the in situ measurements, yielding an R^2 of 0.98, RMSE of 21.94 Wm^{-2}, and Bias of 15.66 Wm^{-2}. However, there was a tendency for overestimation, particularly at high values, when $DSR_{daily\text{-}rugged}$>300 Wm^{-2}.

The accuracy of the estimated $DSR_{daily\text{-}rugged}$ for each of the six sites is presented in Fig. 11a–f, showing that an overestimation in $DSR_{daily\text{-}rugged}$ at high values happened nearly at every site but to different extents. For instance, $DSR_{daily\text{-}rugged}$ was overestimated the least at sites 7 and 6, with their Biases of 6.67 and 8.04 Wm^{-2}, respectively, and the most at sites 4 and 2, with Biases of 25.60 and 22.11 Wm^{-2}, respectively. These results were consistent with those in Fig. 9, and further indicated the need to correct the uncertainty caused by the shadow in estimating $DSR_{daily\text{-}rugged}$, especially for western slopes.

Afterwards, all TCSM $DSR_{daily\text{-}rugged}$ estimates were corrected using the shadow correction method (Eq. (12)). The results shown in Fig. 12 demonstrate that the final estimates and ground measurements were very close to the 1:1 line, even at high values. Compared to Fig. 10, the overall validation accuracy of the shadow-corrected TCSM $DSR_{daily\text{-}rugged}$ estimates was substantially improved, with the RMSE and Bias reduced by 12.25 and 14.73Wm^{-2}, respectively.

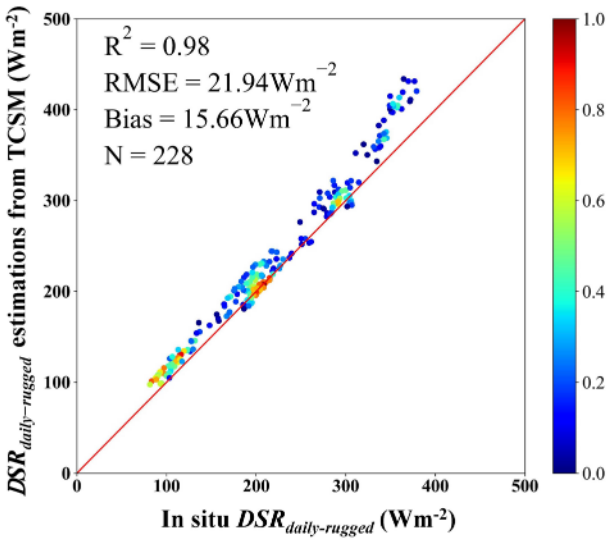

Fig. 10. Overall validation accuracy of the TCSM $DSR_{daily\text{-}rugged}$ estimations for clear days by taking the $DSR_{rugged\text{-}max}$ measurements as the model input.

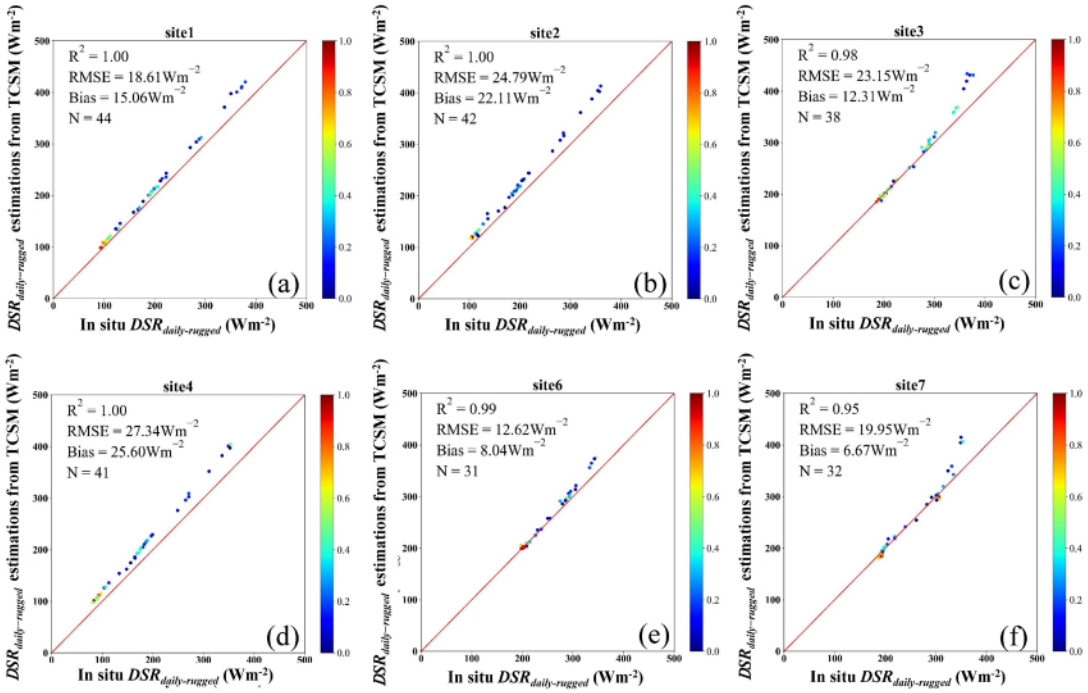

Fig. 11. Same as Fig. 10 but for six mountainous sites: (a) site 1, (b) site 2, (c) site 3, (d) site 4, (e) site 6, and (f) site 7.

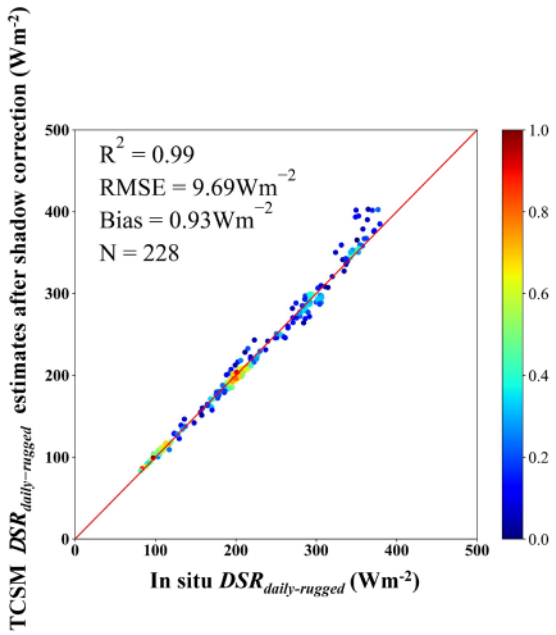

Fig. 12. Same as Fig. 10 but after shadow correction.

2) $DSR_{rugged\text{-}max}$ from the remotely sensed product

Two typical remotely sensed products, CERES4 and MCD18, providing $D_{dir\text{-}ins\text{-}flat}$, $D_{dif\text{-}ins\text{-}flat}$, and $DSR_{ins\text{-}flat}$ at the determined t_{rugged_max}, were used to calculate the $DSR_{rugged\text{-}max}$ first, which were then taken as the inputs for TCSM to calculate $DSR_{daily\text{-}rugged}$ for clear days. As introduced in Section III *A.* 2), there are two methods to estimate the $DSR_{rugged\text{-}max}$. For MCD18, the $DSR_{rugged\text{-}max}$ values were only obtained from the calculated $DSR_{rugged}(t_{overpass})$ according to Eq. (11), which, in turn, was calculated by Eq. (10). In the case of CERES4, the $DSR_{rugged\text{-}max}$ could be calculated at the exact t_{rugged_max} according to Eq. (10) after being resampled, or it could be retrieved in the same manner as MCD18 without resampling. Note that when multiple $DSR_{rugged\text{-}max}$ estimates were available, only the highest one was used to compute $DSR_{daily\text{-}rugged}$. Hence, the TCSM $DSR_{daily\text{-}rugged}$ estimates, with the three kinds of inputs from MCD18, CERES4, and resampled CERES4 after shadow correction, were validated against a common set of ground measurements (No. of samples=145). The results are presented in Fig. 13a–c, respectively.

Generally, the accuracy of the three results was satisfactory and their estimates were distributed close to the 1:1 line, and their RMSE values ranging from 12.60 ~ 18.67 Wm^{-2}, and the magnitude of biases ranging from 5.53 ~ 9.93 Wm^{-2}. Against the same validation samples, the daily DSR from the original MCD18 and CERES4 showed much lower accuracy, yielding the RMSEs of 64.51 and 63.60 Wm^{-2}, Biases of –36.93 and –38.58 Wm^{-2}, and R^2 values of 0.44 and 0.46, respectively. Hence, the performance of the $DSR_{daily\text{-}rugged}$ estimated from the newly proposed method in applications with different remotely sensed products was superiority. Specifically, the accuracy of the shadow-corrected TCSM $DSR_{daily\text{-}rugged}$ estimates from the $DSR_{rugged\text{-}max}$ calculated from MCD18 and CERES4 (Fig. 13a–b) were more accurate than those from the resampled CERES4 (Fig. 13c), yielding RMSEs of 12.60, 14.03, and 18.67 Wm^{-2}, Biases of –7.17, 5.53, and –9.93 Wm^{-2}, and R^2 values of 0.98, 0.97, and 0.95, respectively. Thereby, the uncertainty in the estimated $DSR_{rugged\text{-}max}$, which has major influence on the calculation of $DSR_{daily\text{-}rugged}$, was smaller from the interpolation method, and the lower uncertainty in the estimated $DSR_{rugged\text{-}max}$ retrieved according to Eq. (11) suggested that using it for subsequent calculations reduces uncertainty. Comparing the TCSM $DSR_{daily\text{-}rugged}$ estimates from MCD18 (Fig. 13a) and CERES4 (Fig. 13b), the former showed slightly better performance, with an RMSE decreased by 1.43Wm^{-2}. However, MCD18 showed an underestimation (Bias= –7.17 Wm^{-2}), while CERES4 showed an overestimation (Bias=5.53 Wm^{-2}). After comparing with the accuracy of the TCSM $DSR_{daily\text{-}rugged}$ estimates but taking the in-situ measured $DSR_{rugged\text{-}max}$ as the input against the same samples (RMSE=6.79 Wm^{-2}, Bias=−0.77 Wm^{-2}, R^2=0.99), it could be inferred that the uncertainty of the estimated $DSR_{daily\text{-}rugged}$ resulted from the $DSR_{rugged\text{-}max}$ calculated from MCD18 and CERES4 was 46.11% and 51.6%, respectively, and this uncertainty of $DSR_{rugged\text{-}max}$ was possibly caused by the product itself [57-60] and DCF method. Accordingly, the performance of the product itself and its different spatial resolutions also need to be taken into account in estimating $DSR_{daily\text{-}rugged}$. The more accurate of the product, the more accurate of TCSM estimates.

In summary, TCSM performed very well in both DSR_{rugged} simulation and $DSR_{daily\text{-}rugged}$ estimation over rugged terrain with inputs either from measurements or products.

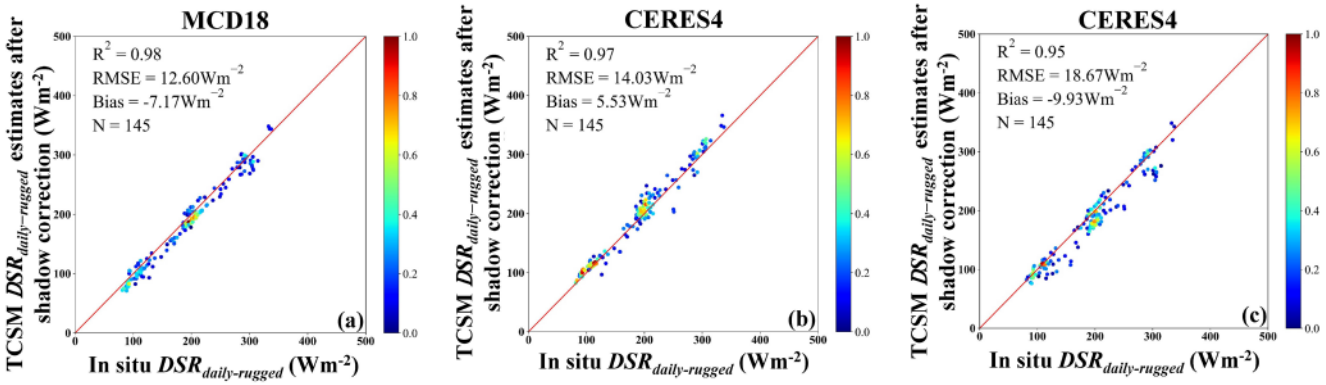

Fig. 13. Overall validation accuracy of the shadow-corrected TCSM $DSR_{daily\text{-}rugged}$ estimates against the in situ measurements by using the common validation samples from (a) MCD18, (b) CERES4, and (c) resampled CERES4 as the inputs.

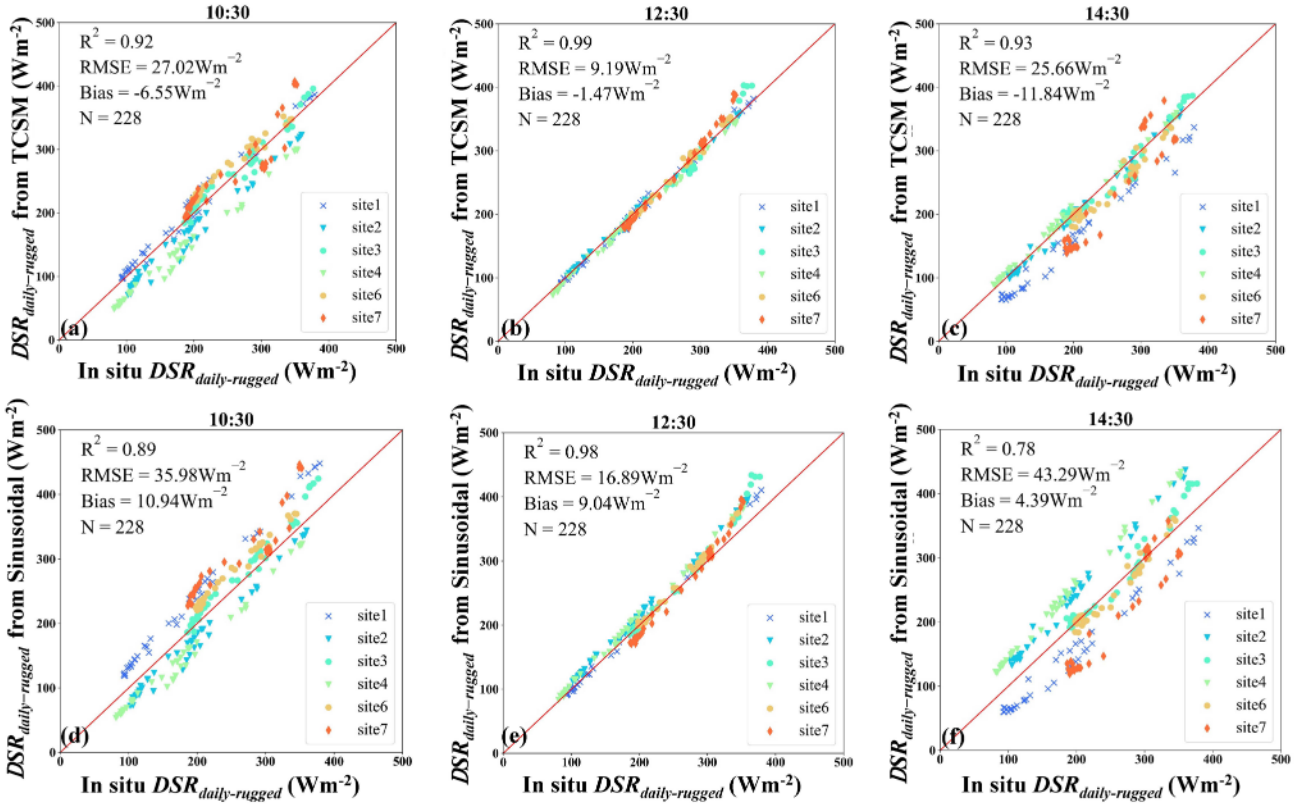

Fig. 14. Accuracy of the shadow corrected $DSR_{daily\text{-}rugged}$ estimation from TCSM and the Sinusoidal model over the same in situ measurements through $DSR_{ins\text{-}rugged}$ at each of times (10:30, 12:30 ,and 14:30hrs). (a–c) TCSM after shadow correction validation result at three times, (d–f) sinusoidal model over a flat surface at three times.

C. Comparison with the Sinusoidal Model

To better assess the temporal expansion capability of TCSM, we computed $DSR_{daily\text{-}rugged}$ by expanding the $DSR_{ins\text{-}rugged}$ measurements taken at 10:30hrs, 12:30hrs, and 14:30hrs using both TCSM and Sinusoidal model. Before that, the $DSR_{rugged\text{-}max}$ should be calculated at first from the in-situ $DSR_{ins\text{-}rugged}$ at the three moments. For TCSM, the $DSR_{rugged\text{-}max}$ was computed by Eq.(11), while for the Sinusoidal model, the $DSR_{rugged\text{-}max}$ was computed by referring to Bisht et al. [31-33].

After shadow correction, the validation results of the two models for the three times are presented in Fig. 14. From the six plots, the shadow-corrected $DSR_{daily\text{-}rugged}$ estimates from TCSM (Fig. 14a–c) outperformed those from Sinusoidal model (Fig. 14d–f), showing higher and more robust accuracy, yielding RMSEs ranging from 9.19 to ~27.02 Wm^{-2} and 16.89 to ~43.29 Wm^{-2}, and Biases ranging of –1.47~ –11.84 Wm^{-2} and 4.39~10.94 Wm^{-2}, respectively. Among all results, the estimates from $DSR_{ins\text{-}rugged}$ at 12:30hrs (Fig. 14b and e) exhibit greater accuracy than those from other moments for both models, with the best ones from TCSM yielding an RMSE of 9.19 Wm^{-2}, Bias of −1.47 Wm^{-2}, and R^2 of 0.99. This is consistent with previous findings that showed that the $DSR_{ins\text{-}rugged}$ at noontime related to the $DSR_{daily\text{-}rugged}$ the closest [10, 14]. Moreover, combining the results before shadow correction (not shown here) shows that TCSM has a tendency to underestimate the $DSR_{daily\text{-}rugged}$, and vice versa for Sinusoidal model, especially for sites on the western slope in the morning and the sites on the eastern slope in the afternoon.

Therefore, all results demonstrate the superior ability of TCSM, especially in $DSR_{daily\text{-}rugged}$ estimation. TCSM is more suitable to be applied over rugged terrain.

V. Conclusion and Discussions

Given the significance of DSR, many algorithms and products have been developed for obtaining DSR. However, few of them take topographic effects into account; thus, the estimated DSR cannot satisfy the application requirements over mountainous regions. To address this issue, the variations of DSR_{rugged} under clear sky and their relationships with various terrain factors have been carefully analyzed using ground measurements collected from the Chengde Experimental Area to develop a new terrain correction model for DSR_{rugged} estimation named Terrain Correction Sinusoidal Model (TCSM).

TCSM assumes that on clear days, DSR_{rugged} follows a pseudo sinusoidal curve, whose maximum value ($DSR_{rugged\text{-}max}$) and time ($t_{rugged\text{-}max}$) are adjusted from the theoretical DSR sine curve from a flat surface under the same conditions based on A, S, and other terrain factors. Hence, the accurate determination of $DSR_{rugged\text{-}max}$ and especially $t_{rugged\text{-}max}$ is crucial for a satisfactory TCSM. We found that the changes of $t_{rugged\text{-}max}$ were majorly affected by A. We established its qualitative relationship through the relationships between $t_{rugged\text{-}max}$ and $t_{us\text{-}max}$ and its variations with A. As long as the $t_{rugged\text{-}max}$ is known,

the $DSR_{rugged\text{-}max}$ can be obtained from measurements or calculated from products with the DCF method. With TCSM, the theoretical daytime clear-sky DSR_{rugged} and the corresponding $DSR_{daily\text{-}rugged}$ can be estimated using minimal measurements or products that provide the $D_{dir\text{-}ins\text{-}flat}$, $D_{dif\text{-}ins\text{-}flat}$, and $DSR_{ins\text{-}flat}$. Comparisons with ground measurements showed that the DSR_{rugged} simulations from TCSM generally agree very well, but shadow effects near sunrise and sunset need to be taken into account. Therefore, we propose a shadow correction method that reduces the influence of terrain-caused shadow effects on TCSM $DSR_{daily\text{-}rugged}$ estimates by correlating estimation residuals with shadow occurrence and duration.

After validation against ground measurements, the performance of TCSM in estimating $DSR_{daily\text{-}rugged}$ was fully evaluated using either measurements or products as inputs. When using measurements, the shadow-corrected TCSM $DSR_{daily\text{-}rugged}$ estimates for clear days exhibited a satisfactory accuracy, with RMSE of 9.69 Wm^{-2}, Bias of 0.93 Wm^{-2}, and R^2 of 0.99. Additionally, TCSM was further compared with the Sinusoidal model by taking the measurements at 10:30, 12:30, and 14:30hrs as inputs. The results demonstrated that TCSM outperformed the Sinusoidal model, with a higher and more robust accuracy, yielding RMSEs in the range of 9.19~27.02 and 16.89~43.29 Wm^{-2} and Bias ranging from –1.47~ –11.84 and 4.39~10.94 Wm^{-2}, respectively. Similarly, when the inputs were from two remotely sensed products, CERES4 and MCD18, the accuracy of the two shadow-corrected TCSM estimated $DSR_{daily\text{-}rugged}$ remained high and improved upon the original products, with the one from MCD18 slightly outperforming that from CERES4, yielding RMSEs of 12.60 and 14.03 Wm^{-2}, Biases of –7.17 and 5.53 Wm^{-2}, and R^2 values of 0.98 and 0.97, respectively.

However, TCSM has several limitations that need to be addressed. First of all, the adaptability of the method to determine $t_{rugged\text{-}max}$ in other places needs to be further examined. Second, the uncertainty of the $DSR_{rugged\text{-}max}$, which can be calculated by the DCF method from products according to Eq. (10), has a remarkable influence on the results. The estimated $DSR_{daily\text{-}rugged}$ is more accurate when more $DSR_{rugged}(t_{sampling/overpass})$ are available or the closer $t_{sampling/overpass}$ is to the $t_{rugged\text{-}max}$. Third, the shadow correction method was built based on limited samples and needs to be refined. Additionally, only single-slope scenarios have been considered in the application of TCSM because of the fine spatial resolution of the SRTM DEM used in this study. More experiments are also needed to support the application of TCSM on surfaces with high albedo and the possibility to expand TCSM for cloud sky.

Overall, this study reveals how DSR varies over rugged terrains, and proposes TCSM, a simple and effective model to simulate DSR_{rugged} and temporally expand it to $DSR_{daily\text{-}rugged}$ under clear sky. The satisfactory results indicate the strong potential of TCSM for practical applications, with further validation and refinements underway.

ACKNOWLEDGMENT

The authors thank NASA and GLASS team for providing the remotely sensed data. The authors thank Prof. Guangjian Yan, Prof. Xihan Mu, Prof. Donghui Xie, and Mr. Yingji Zhou for providing valuable in situ measurements data in Chengde. This data set was provided by the Chengde Remote Sensing Test Site, State Key Laboratory of Remote Sensing Sciences. We thank the data support from the 'National Earth System Science Data Center, National Science and Technology Infrastructure of China' (https://www.geodata.cn, last accessed 23/Aug/2024)

REFERENCES

[1] H. Letu *et al.*, "A review of the estimation of downward surface shortwave radiation based on satellite data: Methods, progress and problems," *Science China Earth Sciences,* vol. 63, no. 6, pp. 774-789, 2020.

[2] K. Yang, J. He, W. Tang, J. Qin, and C. C. K. Cheng, "On downward shortwave and longwave radiations over high altitude regions: Observation and modeling in the Tibetan Plateau," *Agricultural and Forest Meteorology,* vol. 150, no. 1, pp. 38-46, 2010.

[3] M. Wild, "Decadal changes in radiative fluxes at land and ocean surfaces and their relevance for global warming," *Wiley Interdisciplinary Reviews: Climate Change,* vol. 7, no. 1, pp. 91-107, 2016.

[4] L. Chen *et al.*, "Estimation of surface shortwave radiation components under all sky conditions: Modeling and sensitivity analysis," *Remote Sensing of Environment,* vol. 123, pp. 457-469, 2012.

[5] Y. Ma and R. T. Pinker, "Modeling shortwave radiative fluxes from satellites," *Journal of Geophysical Research: Atmospheres,* vol. 117, no. D23, pp. n/a-n/a, 2012.

[6] S. Liang *et al.*, "A long-term Global LAnd Surface Satellite (GLASS) data-set for environmental studies," *International Journal of Digital Earth,* vol. 6, no. sup1, pp. 5-33, 2013.

[7] M. Decker, M. A. Brunke, Z. Wang, K. Sakaguchi, X. Zeng, and M. G. Bosilovich, "Evaluation of the Reanalysis Products from GSFC, NCEP, and ECMWF Using Flux Tower Observations," *Journal of Climate,* vol. 25, no. 6, pp. 1916-1944, 2012.

[8] K. Wang, X. Zhou, and J. Liiu, "The Effects of Comples Terrain on the Computed Surface Solar short-wave Radiation," (in chi), *Chinese Journal of Atmospheric Sciences,* vol. 28, no. 4, pp. 625-633, 2004.

[9] T. Wang, G. Yan, X. Mu, Z. Jiao, L. Chen, and Q. Chu, "Toward operational shortwave radiation modeling and retrieval over rugged terrain," *Remote Sensing of Environment,* vol. 205, pp. 419-433, 2018.

[10] G. Yan *et al.*, "Temporal Extrapolation of Daily Downward Shortwave Radiation Over Cloud-Free Rugged Terrains. Part 1: Analysis of Topographic Effects," *IEEE Transactions on Geoscience and Remote Sensing,* vol. 56, no. 11, pp. 6375-6394, 2018.

[11] E. B. Tegegne *et al.*, "Estimation of the distribution of the total net radiative flux from satellite and automatic weather station data in the Upper Blue Nile basin, Ethiopia," *Theoretical and Applied Climatology,* vol. 143, no. 1-2, pp. 587-602, 2020.

[12] R. Dubayah and S. Loechel, "Modeling Topographic Solar Radiation Using GOES Data," (in English), *Journal of Applied Meteorology,* vol. 36, no. 2, pp. 141-154, 01 Feb. 1997 1997.

[13] Y. Xian *et al.*, "Can Topographic Effects on Solar Radiation Be Ignored: Evidence From the Tibetan Plateau," *Geophysical Research Letters,* vol. 51, no. 6, 2024.

[14] H. Liang, B. Jiang, J. Peng, S. Li, J. Han, and X. Yin, "Estimating daily surface downward shortwave radiation over rugged terrain without bright surface at 30 m on clear-sky days using CERES data," *International Journal of Digital Earth,* vol. 16, no. 2, pp. 4317-4345, 2023.

[15] M. Olson, S. Rupper, and D. E. Shean, "Terrain Induced Biases in Clear-Sky Shortwave Radiation Due to Digital Elevation Model Resolution for Glaciers in Complex Terrain," *Frontiers in Earth Science,* vol. 7, 2019.

[16] A. Mousivand, W. Verhoef, M. Menenti, and B. Gorte, "Modeling Top of Atmosphere Radiance over Heterogeneous Non-Lambertian Rugged Terrain," *Remote Sensing,* vol. 7, no. 6, pp. 8019-8044, 2015.

[17] Z. Xu, H. Luo, T. Zhao, H. Ma, H. Zhang, and J. Gao, "Direct distribution of solar radiation in complex terrain base on GIS," (in chi), *Science of Soil and Water Conservation,* vol. 12, no. 3, pp. 113-118, 2014.

[18] T. Zhou, Z. Wang, H. Qin, and Y. Zeng, "Remote sensing extraction of geothermal anomaly based on terrain effect correction. ," *Journal of Remot Sensing (Chinese)*, vol. v.24, no. 03, pp. 55-66, 2020.

[19] P. Huang, W. Zhao, and A. Li, "Estimation of Solar Radiation and Its Spatio-temporal Distribution Characteristics in the Mountainous Area of Western Sichuan," *Journal of Mountain,* vol. 35, no. 03, pp. 420-428, 2017.

[20] Y. Zhang, X. Qin, X. Li, J. Zhao, and Y. Liu, "Estimation of Shortwave Solar Radiation on Clear-Sky Days for a Valley Glacier with Sentinel-2 Time Series," *Remote Sensing,* vol. 12, no. 6, 2020.

[21] R. Pimentel, C. Aguilar, J. Herrero, M. Pérez-Palazón, and M. Polo, "Comparison between Snow Albedo Obtained from Landsat TM, ETM+ Imagery and the SPOT VEGETATION Albedo Product in a Mediterranean Mountainous Site," *Hydrology,* vol. 3, no. 1, 2016.

[22] S. Wu, J. Wen, D. You, H. Zhang, Q. Xiao, and Q. Liu, "Algorithms for Calculating Topographic Parameters and Their Uncertainties in Downward Surface Solar Radiation (DSSR) Estimation," *IEEE Geoscience and Remote Sensing Letters,* vol. 15, no. 8, pp. 1149-1153, 2018.

[23] F. Li *et al.*, "A physics-based atmospheric and BRDF correction for Landsat data over mountainous terrain," *Remote Sensing of Environment,* vol. 124, pp. 756-770, 2012.

[24] J. Dozier, J. Bruno, and P. Downey, "A faster solution to the horizon problem," *Computers & Geosciences,* vol. 7, no. 2, pp. 145-151, 1981.

[25] R. Dubayah, "Estimating Net Solar Radiation Using Landsat Thematic Mapper and Digital 'Elevation Data," *Water Resources Research* vol. 28(9), pp. 2469-2484, 1992.

[26] Y. Ma *et al.*, "Estimation of fine spatial resolution all-sky surface net shortwave radiation over mountainous terrain from Landsat 8 and Sentinel-2 data," *Remote Sensing of Environment,* vol. 285, 2023.

[27] G. Yan *et al.*, "An Operational Method for Validating the Downward Shortwave Radiation Over Rugged Terrains," *IEEE Transactions on Geoscience and Remote Sensing,* pp. 1-18, 2020.

[28] Y. Zhang, X. Li, and Y. Bai, "An integrated approach to estimate shortwave solar radiation on clear-sky days in rugged terrain using MODIS atmospheric products," *Solar Energy,* vol. 113, pp. 347-357, 2015.

[29] W. Wang, G. Yin, W. Zhao, F. Wen, and D. Yu, "Spatial Downscaling of MSG Downward Shortwave Radiation Product Under Clear-Sky Condition," *IEEE Transactions on Geoscience and Remote Sensing,* vol. 58, no. 5, pp. 3264-3272, 2020.

[30] L. Roupioz, L. Jia, F. Nerry, and M. Menenti, "Estimation of Daily Solar Radiation Budget at Kilometer Resolution over the Tibetan Plateau by Integrating MODIS Data Products and a DEM," *Remote Sensing,* vol. 8, no. 6, 2016.

[31] G. Bisht and R. L. Bras, "Estimation of net radiation from the MODIS data under all sky conditions: Southern Great Plains case study," *Remote Sensing of Environment,* vol. 114, no. 7, pp. 1522-1534, 2010.

[32] G. Bisht and R. L. Bras, "Estimation of Net Radiation From the Moderate Resolution Imaging Spectroradiometer Over the Continental United States," *IEEE Transactions on Geoscience and Remote Sensing,* vol. 49, no. 6, pp. 2448-2462, 2011.

[33] G. Bisht, V. Venturini, S. Islam, and L. Jiang, "Estimation of the net radiation using MODIS (Moderate Resolution Imaging Spectroradiometer) data for clear sky days," *Remote Sensing of Environment,* vol. 97, no. 1, pp. 52-67, 2005.

[34] Y. Zhou *et al.*, "Estimation of Daily Average Downward Shortwave Radiation over Antarctica," *Remote Sensing,* vol. 10, no. 3, 2018.

[35] M. Mikofski. (2022). *Solar Position Calculator* [Online]. Available: https://www.mathworks.com/matlabcentral/fileexchange/58405-solar-position-calculator.

[36] Y. Ma *et al.*, "Landsat snow-free surface albedo estimation over sloping terrain: Algorithm development and evaluation," *IEEE Transactions on Geoscience and Remote Sensing,* pp. 1-1, 2022.

[37] D. Wang, S. Liang, Y. Zhang, X. Gao, M. G. L. Brown, and A. Jia, "A New Set of MODIS Land Products (MCD18): Downward Shortwave Radiation and Photosynthetically Active Radiation," *Remote Sensing,* vol. 12, no. 1, 2020.

[38] X. Zhang, S. Liang, M. Wild, and B. Jiang, "Analysis of surface incident shortwave radiation from four satellite products," *Remote Sensing of Environment,* vol. 165, pp. 186-202, 2015.

[39] B. Tang, Z.-L. Li, and R. Zhang, "A direct method for estimating net surface shortwave radiation from MODIS data," *Remote Sensing of Environment,* vol. 103, no. 1, pp. 115-126, 2006.

[40] D. A. Rutan *et al.*, "CERES Synoptic Product: Methodology and Validation of Surface Radiant Flux," *Journal of Atmospheric and Oceanic Technology,* vol. 32, no. 6, pp. 1121-1143, 2015.

[41] N. F. Liu *et al.*, "A statistics-based temporal filter algorithm to map spatiotemporally continuous shortwave albedo from MODIS data," *Hydrology and Earth System Sciences,* vol. 17, no. 6, pp. 2121-2129, 2013.

[42] Q. Liu *et al.*, "Preliminary evaluation of the long-term GLASS albedo product," *International Journal of Digital Earth,* vol. 6, no. sup1, pp. 69-95, 2013.

[43] Y. Qu, Q. Liu, S. Liang, L. Wang, N. Liu, and S. Liu, "Direct-Estimation Algorithm for Mapping Daily Land-Surface Broadband Albedo From MODIS Data," *IEEE Transactions on Geoscience and Remote Sensing,* vol. 52, no. 2, pp. 907-919, 2014.

[44] T. He, S. Liang, and D.-X. Song, "Analysis of global land surface albedo climatology and spatial-temporal variation during 1981-2010 from multiple satellite products," *Journal of Geophysical Research: Atmospheres,* vol. 119, no. 17, pp. 10,281-10,298, 2014.

[45] T. He, S. Liang, Y. Yu, D. Wang, and Q. Liu, "Greenland surface albedo changes in July 1981–2012 from satellite observations," *Environmental Research Letters,* vol. 8, p. 044043, 12/02 2013.

[46] S. Wang, A. P. Trishchenko, K. V. Khlopenkov, and A. Davidson, "Comparison of International Panel on Climate Change Fourth Assessment Report climate model simulations of surface albedo with satellite products over northern latitudes," *Journal of Geophysical Research,* vol. 111, no. D21, p. D21108, 2006.

[47] E. Rodríguez, C. S. Morris, and J. Belz, "A Global Assessment of the SRTM Performance," *Photogramm Eng Rem S,* vol. 72, pp. 249-260, 2006.

[48] X. Tang *et al.*, "Review on global digital elevation products.," *National Remote Sensing Bulletin,* vol. 25, no. 01, pp. 167-181, 2021.

[49] J. Wen *et al.*, "Characterizing Land Surface Anisotropic Reflectance over Rugged Terrain: A Review of Concepts and Recent Developments," *Remote Sensing,* vol. 10, no. 3, 2018.

[50] Y. Xian, T. Wang, W. Cheng, H. Letu, Y. Du, and W. Leng, "A Uniform Model for Correcting Shortwave Downward Radiation Over Rugged Terrain at Various Scales," *IEEE Transactions on Geoscience and Remote Sensing,* vol. 61, pp. 1-12, 2023.

[51] P. T. Giles, "Remote sensing and cast shadows in mountainous terrain," (in English), *Photogramm Eng Rem S,* vol. 67, no. 7, pp. 833-839, Jul 2001.

[52] Q. Zhou and X. Liu, "Analysis of errors of derived slope and aspect related to DEM data properties," *Computers & Geosciences,* vol. 30, no. 4, pp. 369-378, 2004.

[53] W. Zhao, W. Wang, J. Zhou, L. Ding, and D. Yu, "A Spatial Downscaling Method for Deriving High-Resolution Downward Shortwave Radiation Data Under All-Sky Conditions," *IEEE Transactions on Geoscience and Remote Sensing,* vol. 61, pp. 1-11, 2023.

[54] P. Koronakis, "On the choice of the angle of tilt for south facing solar collectors in the Athens basin area," *Solar Energy,* vol. 36, pp. 217–225, 12/31 1986.

[55] S. Li *et al.*, "Evaluation of nine machine learning methods for estimating daily land surface radiation budget from MODIS satellite data," *International Journal of Digital Earth,* vol. 15, no. 1, pp. 1784-1816, 2022.

[56] B. Jiang *et al.*, "The Hi-GLASS all-wave daily net radiation product: Algorithm and product validation," *Science of Remote Sensing,* vol. 7, 2023.

[57] L. U. Yun-Bo, L. Wang, J.-J. Zhou, N. I. U. Zi-Geng, M. Zhang, and Q. I. N. Wen-Min, "Assessment of the high-resolution estimations of global and diffuse solar radiation using WRF-Solar," *Advances in Climate Change Research,* 2023.

[58] L. Yu, M. Zhang, L. Wang, H. Li, and J. Li, "Characteristics of Aerosols and Clouds and Their Role in Earth's Energy Budget," (in English), *Journal of Climate,* vol. 37, no. 3, pp. 995-1014, 01 Feb. 2024 2024.

[59] Y. Lu *et al.*, "Predicting surface solar radiation using a hybrid radiative Transfer–Machine learning model," *Renewable and Sustainable Energy Reviews,* vol. 173, p. 113105, 2023/03/01/ 2023.

[60] X. Su *et al.*, "Fengyun 4A Land Aerosol Retrieval: Algorithm Development, Validation, and Comparison With Other Datasets," *IEEE Transactions on Geoscience and Remote Sensing,* vol. 61, pp. 1-16, 2023.

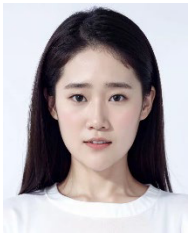

Hui Liang received the B.E. degree in surveying and mapping engineering from Shandong Agricultural University, Taian, China, in 2019, and the M.E. degree in photogrammetry and remote sensing from the State Key Laboratory of Remote Sensing Science, Faculty of Geographical Science, Beijing Normal University, Beijing, China, in 2022. She is currently pursuing the Ph.D. degree with Wuhan University, Wuhan, China.

Her main research interests include surface parameters estimation of energy budget by using remote sensing data.

Bo Jiang (Member, IEEE) received the B.S. degree in mapping and surveying engineering from Central South University, Changsha, China, in 2006, and the M.E. degree in cartography and geographical information system and the Ph.D. degree from Beijing Normal University, Beijing, China, in 2009 and 2012, respectively. From 2010 to 2012, she was a joint Ph.D. Student with the Department of Geographical Sciences, University of Maryland at College Park, College Park, MD, USA. She is with the Faculty of Geographical Science, Institute of Remote Sensing Science and Engineering, Beijing Normal University.

Her research interests include surface net radiation estimation by using remote sensing data, time series analysis, assessing the impacts of the land cover change on the climate from various observations, and the application of remote sensing products.

Shunlin Liang (Fellow, IEEE) received the Ph.D. degree from Boston University, Boston, MA, USA. He is a Professor with the Department of Geographical Sciences, University of Maryland, College Park, MD, USA. He published over 390 SCI indexed peer-reviewed journal article, 42 book chapters, and nine special issues on different journals. He authored/edited seven books and four of which were translated in Chinese, such as "*Quantitative Remote Sensing of Land Surfaces*" (Wiley, 2004), "*Advances in Land Remote Sensing: System, Modeling, Inversion and Application*" (Springer, 2008), "*Advanced Remote Sensing: Terrestrial Information Extraction and Applications*" (Academic Press, 2012, 2019), "*Global LAnd Surface Satellite (GLASS) Products: Algorithms, Validation and Analysis*" (Springer, 2013), "*Land Surface Observation, Modeling and Data Assimilation*" (World Scientific, 2013), and "*Earth's Energy Budget*" (Elsevier, 2017). He has led a team to develop the Global LAns Surface Satellite (GLASS) products that are publicly available at (www.glass.umd.edu) and widely used. His main research interests focus on estimating land surface variables from satellite data, global satellite product generation, Earth's energy balance, and environmental changes.

Dr. Liang was the Editor-in-Chief of the nine-volume books titled "*Comprehensive Remote Sensing*" (Elsevier, 2017). He was an Associate Editor of the IEEE TRANSACTIONS ON GEOSCIENCE AND REMOTE SENSING and is currently the Editor-in-Chief of *Science of Remote Sensing*.

Jianguang Wen received the B.S. degree in geographic information system and the M.S. degree in cartography and geographic information system from Jilin University of China in 2002 and 2005, respectively, and the Ph.D. degree in quantitative remote sensing from the Institute of Remote Sensing Applications, Chinese Academy of Sciences, Beijing, in 2008.

He is currently a Professor with the Aerospace Information Research Institute, Chinese Academy of Sciences. His research interests include the modeling/inversion of land surface bidirectional reflectance distribution function/albedo in rugged terrain from multiple remote sensing sensors and the development of field experiment techniques for land surface parameter validation.

Dr. Wen is a member of the IEEE Geoscience and Remote Sensing Society

Tao He (Senior Member, IEEE) received the B.E. degree in photogrammetry and remote sensing from Wuhan University, Wuhan, China, in 2006, and the Ph.D. degree in geography from the University of Maryland, College Park, MD, USA, in 2012. He is a Professor with the School of Remote Sensing and Information Engineering, Wuhan University, and also with the Department of Geographical Sciences, University of Maryland.

His research interests include surface anisotropy and albedo modeling, data fusion of satellite products, and long-term regional and global surface radiation budget analysis.

Xiaotong Zhang received the B.E. degree in cartography and geographical information engineering from Wuhan University, Wuhan, China, in 2004, and the M.E. degree in cartography and cartography and geographical information system and the Ph.D. degree from Wuhan University, Wuhan, China, in 2006 and 2010, respectively. From 2008 to 2010, he was a joint Ph.D. Student with the Department of Geographical Sciences, University of Maryland at College Park, College Park, MD, USA. He is with the Faculty of Geographical Science, Institute of Remote Sensing Science and Engineering, Beijing Normal University.

His research interests include shortwave radiation estimation using remotely sensed data.

Jianghai Peng received a M.S. degree in cartography and geographical information system from the State Key Laboratory of Remote Sensing Science, Faculty of Geographical Science, Beijing Normal University, Beijing, China, in 2021. He is currently pursuing the Ph.D. degree at Arizona State University.

His main research interests include the application of remote sensing in ocean ecology.

Shaopeng Li received the B.S. degree in surveying and mapping engineering from Hebei University of Technology, Tianjin, China, in 2019, and the M.S. degree in photogrammetry and remote sensing from Beijing Normal University, Beijing, China, in 2022. He is currently pursuing the Ph.D. degree in climate science from University of Bern, Bern, Switzerland.

His research interests include Albedo coupling with vegetation dynamics over global, Albedo and radiation inversion, and AI in quantitative remote sensing.

Jiakun Han received the B.E. degree in surveying and mapping engineering from Shandong Agricultural University, Taian, China, in 2020, and a M.S. degree in cartography and geographical information system from the State Key Laboratory of Remote Sensing Science, Faculty of Geographical Science, Beijing Normal University, Beijing, China, in 2023.

Her main research interests include the temporal extrapolation methods in net radiation.

Xiuwan Yin received the B.S. degree in Geographical Information Science from Jiangxi Normal University, Jiangxi, China, in 2021. She is pursuing the M.S. degree in cartography and geographical information system with the State Key Laboratory of Remote Sensing Science, Faculty of Geographical Science, Beijing Normal University, Beijing, China.

Her research interests focus on the effect of vegetation cover change on land surface energy balance and regional climate response.